Journal Of Semiconductor Science And Technology

Volume No. 12

Issue No. 1

January - April 2024

ENRICHED PUBLICATIONS PVT. LTD

S-9, IInd FLOOR, MLU POCKET,
MANISH ABHINAV PLAZA-II, ABOVE FEDERAL BANK,
PLOT NO-5, SECTOR-5, DWARKA, NEW DELHI, INDIA-110075,
PHONE: - + (91)-(11)-47026006

Journal Of Semiconductor Science And Technology

Aims and Scope

Journal of Semiconductor Science & Technology is a journal of high quality devoted to the publication of original research papers on all aspects of semiconductor research and applications. The journal publishes original research papers on main aspects of experimental and theoretical studies of the properties of semiconductors and their interfaces. Appropriate subjects include but not limited to electrical properties, optical properties, device design, device fabrication, materials processing, materials and device analysis, process monitoring, reliability. Review articles in selected areas are published from time to time.

Journal Of Semiconductor Science And Technology

Journal Of Semiconductor Science And Technology

(Volume No. 12, Issue No. 1, January - April 2024)

Contents

The Energetically Favorable Configurations For Forming Silicon Nanostructures

R.Khatri*
*Department of Physics, DAV College, Abohar India

ABSTRACT

Using density functional calculations, we show that the energetically favourable configurations of silicon monoxide clusters (SiO)n for n ≥ 5facilitate the nucleation and growth of silicon nanostructures as the clusters contain sp3 silicon cores surrounded by silicon oxide sheaths. The frontier orbitals of (SiO)n clusters are localized to a significant degree on the silicon atoms on the surface, providing high reactivity for further stacking with other clusters. The oxygen atoms in the formed larger clusters prefer to migrate from the centers to the exterior surfaces, leading to the growth of sp3silicon cores.

Introduction

Silicon (Si) suboxide clusters have drawn much attention since they play a crucial role in the oxide assisted growth of silicon nanowires (SiNWs) [1-3] . Their predominant role in the synthesis of SiNWs has been revealed in many experiments in which high yields of nanowires surrounded by SiO_2 sheaths were obtained by either thermal evaporation or laser ablation of Si powder mixed with SiO2 or simply SiO [1-3]. Interestingly, the maximum yield of SiNWs compared to that from a metal containing target was achieved when the chemical compositions of silicon and oxygen in the source are equal, whereas hardly any or no SiNWs can be obtained with pure SiO_2 materials [2]. This indicates clearly that gasphase Si suboxide clusters, especially silicon monoxide clusters, generated by evaporation of sources containing Si and SiO2 or SiO, play an important role in the nucleation and growth of SiNWs. Obviously, the mechanism of oxide assisted growth is quite different from the classical vapor liquid solid mechanism involved in metal catalyzed growth [1,4,5]. To understand the oxide assisted formation process, the exploration of silicon oxide clusters with wider ranges of sizes and oxygen rations is highy desirable.

Small silicon oxide clusters SinOm (n,m = 1-8) have been studied both experimentally and theoretically [6-10]. Planar and buckled ring configurations have been oxygen rich clusters were predicted to be rhombuses arranged in a chain with adjacent ones perpendicular to each other. Although Si suboxide clusters are shown to be highly reactive to bond with other clusters and prefer to form Si-Si bonds based

on the analysis of their frontier orbitals [11], no direct theoretical evidence on te formation of sp3 Si cores inside Si oxide clusters has been presented so far due to insufficient knowledge of Si suboxide clusters with a wider range of sizes. However, such clusters are expected to lead to nucleation of Si nanocrystals via the combination of small Si suboxide clusters. We study the energetically most favourable configurations of Si monoxide clusters (SiO)n for n ranging from 3 to 21 and their corresponding electronic properties calculated using density functional theory (DFT), with the aim to elucidate the oxide assisted growth process of SiNWs.

Calculations

Our calculations were conducted at DFT level using the GAUSSIAN 98 package [12] and a SIESTA code [13]. B3LYP/6-31G* of DFT have accurately reproduced the properties of SinOm obtained from both experiments and other high level calculations [6,9,10,14]. SIESTA adopts a localized linear combination of numerical atomic orbital basis sets for the description of valance electrons and norm conserving nonlocal pseudopotentials[15] for the atomic core to improve its computational efficiency. The generalized gradient approximation corrections in the form of Perdew, Burke, and Ernzerhof[16] and the double-ζ plus polarization orbital basis sets were employed throughout the SIESTA calculations. The energetically more favourable structures of (SiO)n clusters were searched with various designed initial configurations which were first annealed at 500 K for 2 ps with a Verlet algorithm using SIESTA with a force tolerance less than 0.01 eV/Å. For small (SiO)n (n<11), the relaxed structures using SIESTA were further optimized using B3LYP/6-31G* calculations were performed with the structures optimized by SIESTA based on the finding that the optimized configurations obtained using B3LYP/6-31G* and SIESTA were very close, with the difference in bond lengths and bond angles being less than 1.7% and 3.6%, respectively, for small clusters, Binding energies were calculated from the difference between the total energy of a cluster and the energies of the corresponding isolated spin polarized Si and O atoms.

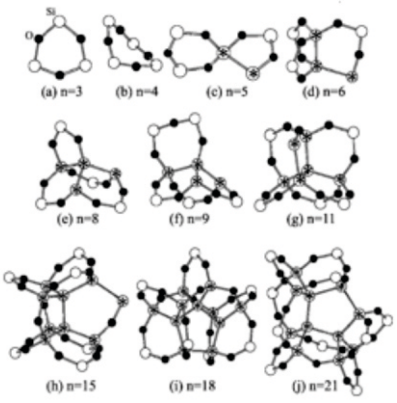

FIG.1. The structures of silicon monoxide clusters (SiO)n, The open circles containing starts represent Si atoms in Si cores, the open circles containing stars represent Si atoms in Si cores, the open circle the unsaturated Si atoms, and the filled smaller circles O atoms.

The energetically most favorable configurations of the $(SiO)_3$ and $(SiO)_4$ clusters are the planar and buckled-ring configurations [6,17], respectively, as shown in Fig. 1. For the $(SiO)_5$ cluster, the one involving a Si-Si bond (Si cored), as shown in Fig. 1, is energetically more favorable than the buckled structure. The total binding energies of buckled and Si-cored isomers at different levels of calculations are given in Table I. The data clearly show that the Si-cored structure is more stable than the buckled configuration by about 0.3 to 0.4 eV due to the formation of a four-coordinated Si atom in the center of the cluster. The energetically most favorable configurations of larger representative clusters (SiO)n for n ranging from 6 to 21 are presented in Fig. 1 as well. The following characteristics are observed: (1) a Si core (represented by the open circles containing stars in Fig. 1 surrounded by a silicon oxide sheath is involved; (2) the Si-Si bonds prefer to form in the center rather than at the cluster surface so as to reduce the strain caused; (3) most of the Si atoms in the Si core have three or four coordinates with Si-Si-Si bond angles close to 109o (the value found in silicon crystal), which is quite different from that of pure Si clusters of the same size [18]; (4) with increasing cluster size, the size of the Si core increases and the fraction of Si atoms with three and four coordinates increases correspondingly, making the cluster more stable; and (5) starting at n = 18 all of the Si atoms in Si cores are four- coordinated, indicating the formation of sp3 Si cores similar to the configuration in the Si crystal. Figure 2 depicts the binding energies of (SiO)n clusters containing Si cores as a function of n, together with those containing buckled structures. It is clear that: (1) the configurations containing Si cores become energetically more favorable than the buckled structures for n=5 and larger; and (2) the cluster becomes increasingly more stable with increasing Si core size. As the two structures from n = 5 to n = 8 in Fig. 2 are close in energy, we further estimate their relative population at 900^{o}C (the growth temperature of SiNWs [3] by assuming the process is at equilibrium and described by the Boltzmann factor exp[-E/kT], where k is Boltzmann's constant, E is the energy difference, and T is temperature in Kelvin. The results shown in the inset in Fig. 2 confirm that the structures containing Si cores still play the major role at such a high temperature starting at a size as small as n = 8. To understand the formation of Si cores, we calculated the binding energies of some (SiO)n clusters with the configurations in which an O atom resides in the Si cores. We found that all of these configurations are energetically less favorable than those with the O atom located at the cluster surface, due to the higher strain caused, indicating that they are metastable. Moreover, the difference in binding energy between the metastable structure and the most stable configuration becomes increasingly larger with increasing cluster size. For example, for the $(SiO)_5$ cluster the energy difference is 0.37 eV [Fig. 3(a)], whereas for the $(SiO)_9$ cluster the energy difference increases to 0.90 eV. We considered three different isomers of the $(SiO)_{21}$ cluster with an O atom residing in different sites from the center to the surface of the cluster, as shown in Fig. 3(b). The most stable configuration is the one with O located on its surface with a total binding energy of 211.74 eV, while the binding energy decreases as the O atom moves from the surface into the cluster (from 209.43 to 208.42

eV). Based on these results, we conjecture that the O atom can migrate from the center of the silicon monoxide cluster to its surface via bond switching, resulting in the formation of sp_3 Si core.

TABLE I. Total binding energy (eV) of the isomers of _SiO_5 cluster. "Buckled" was presented in Ref. [17], and "Si-cored" is shown in Fig. 1(c). MP2 refers to MP2/6-31G*; MP2/SIESTA represents MP2/6-31G*//SIESTA; DFT is B3LYP/6-31G*; and DFT/SIESTA stands for B3LYP/6-31G*//SIESTA.

	MP2	MP2/SIESTA	DFT	DFT/SIESTA	SIESTA
Buckled	-46.974	-46.8134	-47.092	-46.8827	-52.1547
Si-cored	-47.4175	-47.2597	-47.397	-27.2419	-52.9616

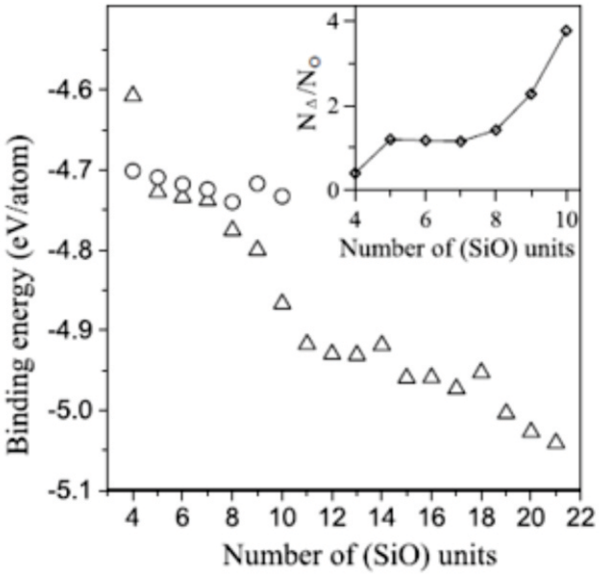

FIG. 2. Binding energy (eV/atom) of (SiO)n clusters versus n. The up triangles are (SiO)n with the Si-cored structure surrounded by a silicon oxide sheath, and open circles are those with buckled-ring structure. The inset shows the relative population of the former (N△) and the latter (No) structures at 900°C.

The estimated migration barrier is about 1.79 eV for the $(SiO)_5$ cluster [see Fig. 3(a)], which is close to the energy barrier (～1:3 eV) of the O atom diffusing in Si crystal in the oxidation process [19]. It is expected that the high strain involved in the (SiO)n cluster may cause the O atom to migrate to the surface. Similarly, the study of SiO_2=Si(100) interfaces showed that stress release via excess atom (Si) emission is essential and universal [20]. The electronic structures of (SiO)n clusters have been analyzed to reveal their chemical reactivity. The energy gaps between the highest occupied molecular orbital (HOMO) and lowest unoccupied molecular orbital are found to be 2.0–4.5 eV, which is much lower than that for silicon dioxide clusters of the same size [9,14], indicating that (SiO)n clusters have higher

chemical reactivity [11]. More importantly, the HOMO is localized to a significant extent on the Si atoms at the cluster surface, as revealed by density-of-state decomposition [11], making these regions the likely reactive sites. The combination of these clusters may easily occur through the Si-Si bonding between them, forming larger clusters. Subsequently, the reconstruction and O migration will give rise to the formation of a (SiO)n cluster containing a large sp3 Si core. However, this process cannot be revealed with molecular dynamics simulations due to insufficient simulation time (computations using currently available facilities could be performed at most for a few picoseconds) and the high energy barrier of O migration in (SiO)n clusters. Nonetheless, the migration of O atoms in (SiO)n clusters could be driven by the heat released in the reconstruction process and/or by the strain involved in the large clusters formed by the combination of small clusters.

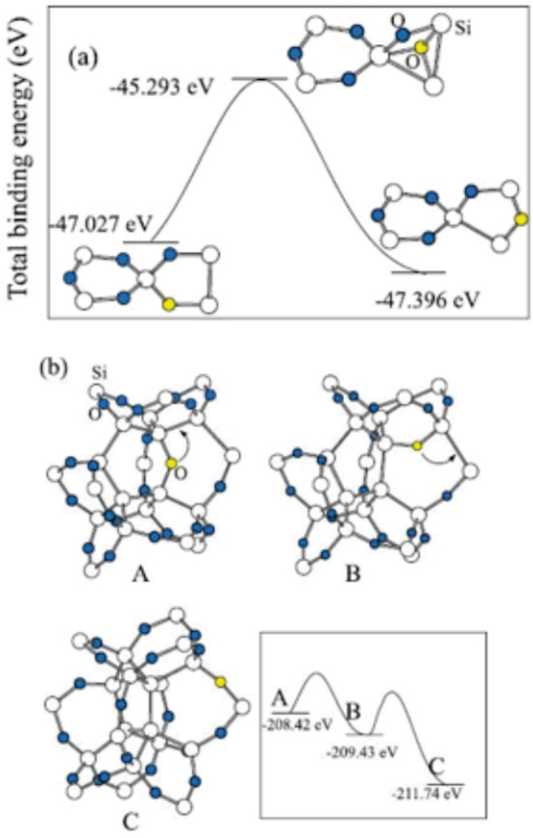

FIG.3. (color). Possible path of O atom migration from the center of a (SiO)n cluster to its surface; (a) $(SiO)_5$ and (b) $(SiO)_{21}$.

The structural transition to the diamond structure in Si clusters as the cluster size exceeds a critical value (300– 500 atoms) has been revealed both experimentally and theoretically [18,21,22]. Similarly, the possible structural transitions are deduced here for (SiO)n clusters, making these clusters act as nuclei or precursors for the subsequent growth of Si nanostructures.

Considering that the Si atoms in the Si core have the character of sp_3 hybridization similar to that in Si

crystal, the critical size [n = 18; see Fig. 1(I)] for the structural transition is seen to be much smaller than that of pure Si clusters (400–500 atoms) [18]. It is also noteworthy that the structure of the sp3 Si core surrounded by the silicon oxide sheath in our calculation is still slightly different from the tetrahedral structure in a Si crystal but is more like the hexagonal structure that has been studied theoretically [23] and experimentally [24]. A transition from the hexagonal to the tetrahedral structure may be expected at a certain size so that the (SiO)n clusters are suitable to act as the nucleus and precursor for the subsequent growth of Si nanostructures such as SiNWs. We now discuss the nucleation and growth of Si nanostructures, in particular, SiNWs [2,3], from these clusters. In an experiment using SiO powder or a mixture of Si and SiO2 powder as the source, the evaporated (SiO)n clusters deposited on a substrate would be anchored due to their high reactivity at Si sites. The deposited clusters would act as the nuclei to absorb (SiO)n clusters from the vapor because of their remaining reactive Si atoms facing outwards from the substrate. A Si core would start to form at a size of n=5. The nuclei containing a Si core would grow larger with the assistance of O diffusion from the core to the surface layer during deposition. The O diffusion length depends on the temperature and the crystallographic orientation of the crystalline core formed, leading to the formation of SiNWs with different crystalline orientations such as <110> and <112>, as observed in our experiments [3]. It is worth noting that the above process may be similarly responsible for the ready formation of Si nanocrystals in the sp3 configuration from amorphous SiO [25,26]. To conclude, using DFT calculations we show that the energetically most favorable structures of silicon monoxide clusters (SiO)n for $n \geq 5$ contain a sp3 Si core surrounded by a silicon oxide sheath. Because of their high chemical reactivity, a combination of these clusters may easily take place, forming clusters with a large sp3 Si core via subsequent reconstruction and O migration from the center to the surface of the clusters. The crystalline Si cores thus formed can act as nuclei and precursors for subsequent growth of Si nanostructures.

References

[1] Y. F. Zhang, Y. H. Tang, N. Wang, D. P. Yu, C. S. Lee, I. Bello, and S.T. Lee, Appl. Phys. Lett. 72, 1835 (1998).
[2] N.Wang, Y. F. Zhang, Y. H. Tong, C. S. Lee, and S.T. Lee, Phys. Rev. B 58, R16 024 (1998).
[3] R.Q. Zhang, Y. Lifshitz, and S.T. Lee, Adv. Mater. 15, 635 (2003).
[4] A.M. Morales and C.M. Lieber, Science 279, 208 (1998).
[5] R. S. Wagner and W.C. Ellis, Appl. Phys. Lett. 4, 89 (1964).
[6] S. K. Nayak, B. K. Rao, S. N. Khanna, and P. Jena, J. Chem. Phys. 109, 1245 (1998).
[7] J. R. Chelikowsky, Phys. Rev. B 57, 3333 (1998).
[8] L. S. Wang, J. B. Nicholas, M. Dupuis, H. Wu, and S. D. Colson, Phys. Rev. Lett. 78, 4450 (1997), and references therein.
[9] T. S. Chu, R.Q. Zhang, and H. F. Cheung, J. Phys. Chem. B 105, 1705 (2001).
[10] W. C. Lu, C. Z. Wang, V. Nguyen, M.W. Schmidt, M. S. Gordon, and K.M. Ho, J. Phys. Chem. A 107, 6936 (2003).
[11] R.Q. Zhang, T. S. Chu, H. F. Cheung, N. Wang, and S.T.Lee, Phys. Rev. B 64, 113304 (2001).
[12] M. J. Frisch et al., GAUSSIAN 98, Gaussian, Inc.,Pittsburgh, PA, 1999.

[13] P. Ordejo´n et al., Phys. Rev. B 53, R10 441 (1996); D. Sa´nchez-Portal et al., Int. J. Quantum Chem. 65, 453 (1997); E. Artacho et al., Phys. Status Solidi B 215, 809 (1999); J.M. Soler et al., J. Phys. Condens. Matter 14, 2745 (2002); and references therein.
[14] S.T. Bromley, M. A. Zwijnenburg, and Th. Maschmeyer, Phys. Rev. Lett. 90, 035502 (2003).
[15] N. Troullier and J. L. Martins, Phys. Rev. B 43, 1993 (1991).
[16] J. P. Perdew, K. Burke, and M. Ernzerhof, Phys. Rev. Lett. 77, 3865 (1996); Phys. Rev. Lett. 78, 1396 (1997) and references therein.
[17] R.Q. Zhang, T. S. Chu, and S.T. Lee, J. Chem. Phys. 114, 5531 (2001).
[18] D. K. Yu, R.Q. Zhang, and S.T. Lee, Phys. Rev. B 65, 245417 (2002), and references therein.
[19] K. Kato, T. Uda, and K. Terakura, Phys. Rev. Lett. 80, 2000 (1998).
[20] H. Kageshima and K. Shiraishi, Phys. Rev. Lett. 81, 5936 (1998).
[21] J. R. Chelikowsky, Phys. Rev. Lett. 60, 2669 (1988).
[22] B. Marsen, M. Lonfat, P. Scheier, and K. Sattler, Phys. Rev. B 62, 6892 (2000).
[23] J. D. Joannopoulos and M. L. Cohen, Phys. Rev. B 7, 2644(1973).
[24] Y. Zhang, Z. Iqbal, S. Vijayalakshmi, and H. Grebel, Appl. Phys. Lett. 75, 2758 (1999).
[25] M. Mamiya, M. Kikuchi, and H. Takei, J. Cryst. Growth 237, 1909 (2002).
[26] M. Zacharias, J. Heitmann, R. Scholz, U. Kahler, M. Schmidt, and J. Blasing, Appl. Phys. Lett. 80, 661 (2002).

Study In Application Of Nanotechnology To Achieve Water Repellency

Chinchwade S.S.*, Landage S.M., Bonsule S.*****
*Assoc. Prof., Dept. of Textiles, D.K.T.E's Textile & Egg. Institute, Ichalkaranji, India
**Asstt. Prof., Dept. of Textiles, D.K.T.E's Textile & Egg. Institute, Ichalkaranji, India
***M.Text.(Tech.Text.) candidate, D.K.T.E's Textile & Egg. Institute, Ichalkaranji, India

ABSTRACT

To obtain water repellent polyester non woven fabric. Fabric was treated with silica nano particle and commercially available water repellent agent. Silica nano particle was synthesized by using stobermethod, fabric was treated with silica nano particle and combination of both silica nano particle and water repellent agent and compare.For fabric treated with water repellent agent shows the rating of 80 for 35gpl and fabric treated with combination of both shows the rating of 100 for 35gpl that is super hydrophobic surface.

Key words: Nanoparticles, Nanosilica, Superhydrophobicity, Self-Cleaning, Surface Energy.

Introduction

For many years, people have been attracted by the self-cleaning property of the lotus leaf, and dream to develop man-made super hydrophobic surfaces. Superhydrophobic and self- cleaning surfaces exist widely in nature. Butterfly wings, legs of a water strider and leaves of some plants are good examples. Thanks to the innovation of scanning electron microscopy, today, scientists know the plant's ability to repel water and dirt results from the super hydrophobicity, due to the combination of micrometer-scale hills and valleys and nanometer-scale waxy bumps, in combination with the reduced adhesion between surfaces and particles. A surface with water contact angle large than 150° and a low sliding angle (the critical angle where a water droplet with a certain weight begins to slide down the inclined plate) is usually called a super hydrophobic surface. A combination of low surface energy and adequate surface roughness is necessary to obtain super hydrophobic and superoleophobic surface. High contact angles are achieved by reducing the surface energy of the solid surface and increasing its roughness in an appropriate manner, thus reducing wetting. Techniques involved in developing such surfaces include plasma treatment, chemical etching, chemical vapor deposition, lithography, and so forth. [1, 2, 3, 4]

Principle Of Super Hydrophobicity

Wetting of a solid surface is dominated by three interfacial tensions and can simply be evaluated by the spreading parameters(S).

(1) $S=\gamma SV-(\gamma SL+\gamma SV)$

If the spreading parameter S>0, the liquid tends to spread completely on the solid. While for S<0, the liquid partially wets the solid and forms a spherical cap with a contact angle ΘC, which is usually used for quantitative characterization of the wetting phenomena. The value of the angle is determined by three surface tensions where the chemical potential in the three phases should be at equilibrium. Therefore, the contact angle relationship ΘC derived by balancing the three tension forces onto the solid surface

$$(2)\quad \cos(\theta_C) = \frac{\gamma_{SV} - \gamma_{SL}}{\gamma_{LV}}$$

This is Young's equation for the determination of contact angles. [5]

2. Materials And Methods

2.1. Materials

- Fabric/substrate sample - 100% Polyester Spunlace Nonwoven fabric

Table 1: Fabric specifications

	100% Polyester nonwoven fabric
Fabric thickness (mm)	0.4
GSM	40
Air-permeability ($cm^3/cm^2/s$)	73.2

- **Chemicals used:**

Chemical Name	Function
TEOS (tetraethyl orthosilicate)	Chemicals used for the synthesis of Silica Nanoparticles
Ethanol	
Ammonia	
TUBIGAURD	water repellent agent
Magnesium chloride	stabilizer for water repellent agent
Acetic acid	pH maintainer

2.2 Methods

Synthesis of silica nanoparticles:

The silica nanoparticles were prepared by the modified Stober method of hydrolysis, dehydration and condensation of TEOS as a precursor. Firstly a mixture of 0.2 mol tetraethyl orthosilicate and 2.5 mol ethanol was prepared, then it was mixed with the mixture of 2.0 mol distilled water, 2.5 mol ethanol and 0.05 mol ammonia solution. The synthesis was carried out for 3 hours at 30^0C. The following tables show the chemical composition for the synthesis of silica nanoparticles. [6]

Table 1.1: Recipe for the synthesis of silica nanoparticles

Sr. No	Chemical	Concentration (Mol)	Solution No.
1	TEOS	0.2	Solution 1
2	Ethanol	2.5	
3	Water	2	
4	Ethanol	2.5	Solution 2
5	Ammonium hydroxide	0.05	

Solution 1 + Solution 2 ⟶ Stirring at 30^{0}C for 3 hours.

Sr. No.	TEOS (Mol)	Ethanol (Mol)	Water (Mol)	Ethanol (Mol)	Ammonium hydroxide (Mol)
1	0.2	2.5	2	2.5	0.05

2.2 Application of Silica Nanoparticles and the Water Repellent Agent on polyester nonwoven fabric:

The polyester nonwoven fabric considered as the substrate to be applied is padded with the silica sol that was prepared earlierusing a laboratory padding mangle. The padded fabric samples were then dried at room temperature to maintain residual moisture content 8 – 10%. The dried fabric samples were cured at 140^{0}C for 3min. Then these fabric samples were again padded with the water repellent agent with varying concentration from 15gpl – 40gpl. The padded fabric samples were the dried at room temperature and cured at 140^{0}C for 3min. The following table shows the chemical composition for the water repellent finish.

Table 2: Recipe for Water Repellent finish

Sr.No	Chemical	Concentration
1	TUBIGAURD	15, 20, 25, 30, 35, 40 gpl
2	Magnesium chloride	12 gpl
3	Acetic acid	Add to maintain pH of 4.5 – 5

The following table shows the chemical Composition of water repellent agent and silica nonoparticles for water repellent finish.

Table 3: Composition of water repellent agent and silica nanoparticles for water repellent finish

Sr. No.	TEOS (Mol)	Ethanol (Mol)	Water (Mol)	Ethanol (Mol)	Ammonium hydroxide (Mol)	Water Repellent Agent (gpl)
1	0.2	2.5	2	2.5	0.05	15
2	0.2	2.5	2	2.5	0.05	20
3	0.2	2.5	2	2.5	0.05	25
4	0.2	2.5	2	2.5	0.05	30
5	0.2	2.5	2	2.5	0.05	35
6	0.2	2.5	2	2.5	0.05	40

Each of the fabric samples treated with the silica nanoparticles as per the recipe mentioned above is further treated with the Water Repellent agent of concentrations ranging from 15 – 40 gpl as mentioned in table 2.

Test Standards

Spray Rating TestAATCC 22, ISO 4920	**Air-permeability**– ASTM 738-04
Hydro-static head pressure test	**SEM**– JOEL JSM 636

3. Results And Discussions

3.1 Characterization:-

Scanning Electron Microscope (SEM) is used to characterized the surface morphology of treated fabric. It was observed that, due to the presence of silica nanoparticles fabric shows the scaly appearance on the surface, which made the surface rougher & enhance the water repellency. Figure 1 shows, the SEM image of polyester nonwoven fabric treated with silica nanoparticles & figure 2 shows the SEM image of Polyester Nonwoven fabric treated with both silica nanoparticles and water repellent agent . The figure 2 shows the water repellent agent forms an oily layer on the silica nanoparticles just like lotus leaves. Here silica nanoparticles act as an epidermal cells and water repellent agent as waxy bumps which results in superhydrophobicity on polyester nonwoven fabricfabric.

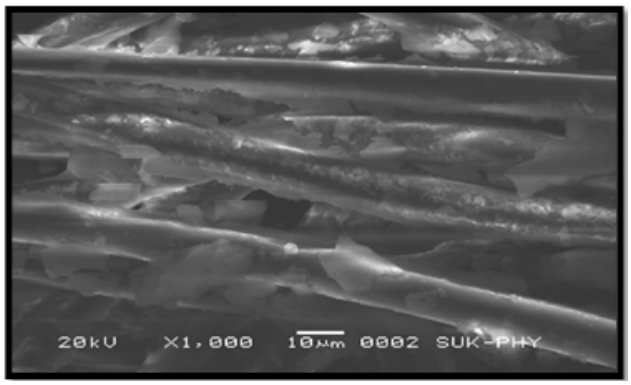

“Figur 1. SEM image of Polyester nonwoven fabric treated with silica nanoparticles”

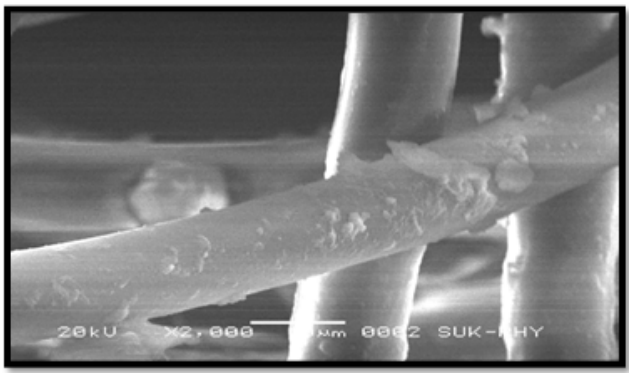

“Figur 2. SEM image of polyester nonwoven fabric treated with both silica nanoparticles and water repellent agent

3.2 Effect of concentration of water repellent Agent on Water Repellency Rating- SprayRating. Spray Rating

"Table 4. Effect of concentration of water repellent Agent on Water Repellency Rating-Spray Rating"

	Values of spray test ratings					
	Water repellent agent					
	15 g/l	20g/l	25 g/l	30 g/l	35 g/l	40 g/l
Finished with silica nano particle and water repellent agent	50	80	100	90	100	100
Finished only with water repellent agent	70	70	80	80	80	90

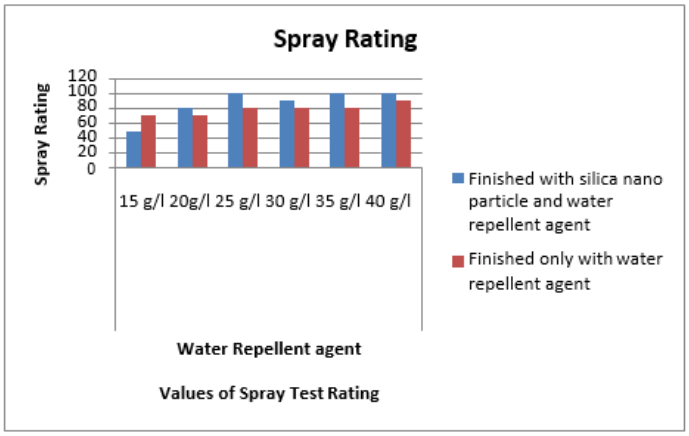

"Figure 4.Effect of concentration of water repellent Agent on Water Repellency Rating-Spray Rating"

From the above table 4 and Figure 4 it is observed that the fabric finished with only water repellent agent shows the increase in water repellency rating from 70 for 15 g/l to 90 for 40 g/l, while fabric finished with combination of water repellent agent and nano silica particle shows increase in spray rating from 50 for 15 g/l to 100 for 40 g/l. The fabric finished with combination of water repellent agent and nano silica particle shows the rating of 50 for 15 g/l, it is because of the random alignment offibres in non woven fabric. From the graph and table it is observed that 25 g/l gives optimum result.

3.3 Effect of Concentration of Water Repellent Agent on Air Permeability.

"Table 5.Effect of Concentration of water Repellent Agent on Air Permeability"

	Values of Air Permeability ($Cm^3/Cm^2/Sec$)					
	Water repellent agent					
	15 g/l	20g/l	25 g/l	30 g/l	35 g/l	40 g/l
Finished with silica nano particle and water repellent agent	68.65	68.56	68.32	68.27	67.82	67.6
Finished only with water repellent agent	72.02	71.76	69.75	71.06	69.9	68.4

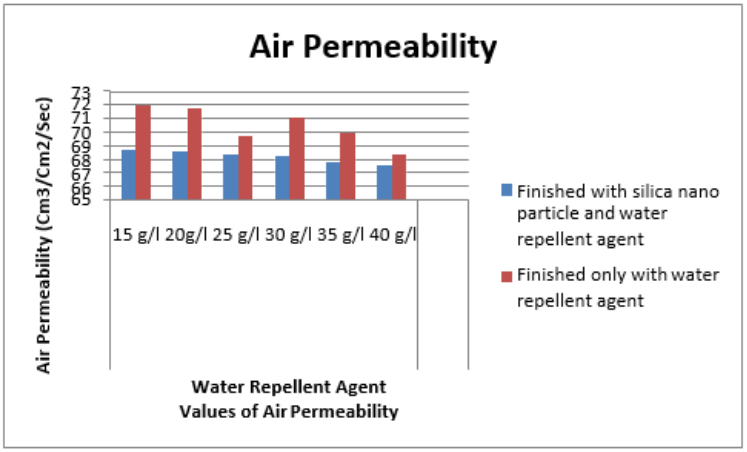

"Figure 5 .Effect of Concentration of water Repellent Agent on Air Permeability"

From the Table 5 and Figure 5, it is observed that, the fabric finished with only water repellent agent shows the decrease in air permeability from 72.02 to 68.4 for the concentration of 15 gpl to 40 gpl of water repellent agent respectively some values are fluctuate in between 20 g/l and 30 g/l this is because of random alignment of fibres in non woven fabric, while the fabric finished with combination of silica nanoparticles and water repellent agent shows decrease in air permeability from 68.65 to 67.60 for the concentration of 15 gpl to 40 gpl of water repellent agent respectively.This may be because; as concentration goes on increasing the film is going to become continuous, which causes decrease in air transmission rate& also the silica nanoparticles help in filling the interstices between fibres.

3.4 Effect of Concentration of Water Repellent Agent on Hydrostatic Head Pressure.

"Table 6. Effect of Concentration of Water Repellent Agent on Hydrostatic Head Pressure."

	Values of Air Hydrostatic Head Pressure (cm)					
	Water repellent agent					
	15 g/l	20g/l	25 g/l	30 g/l	35 g/l	40 g/l
Finished with silica nano particle and water repellent agent	14.43	14.83	15.42	15.43	15.6	15.6
Finished only with water repellent agent	14.2	14.77	15.02	15.33	15.33	15.9

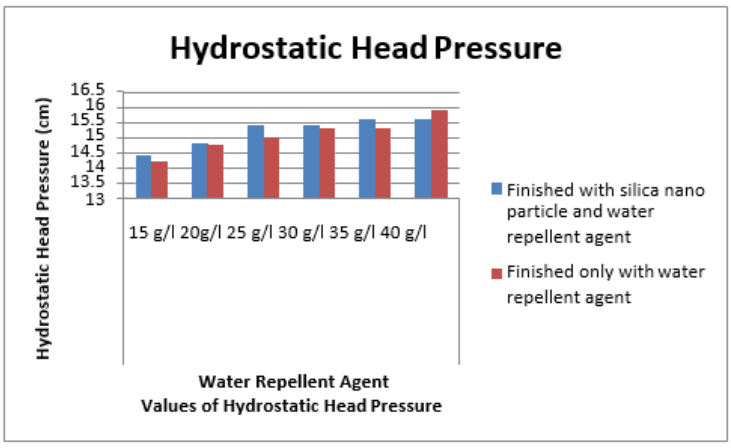

"Figure 6. Effect of concentration of water repellent agent on hydrostatic head pressure."

The above Table 6 and Figure 6 shows that, the fabric finished with only water repellent agent shows the increase in hydrostatic head pressure from 14.20 to 15.33 for water repellent agent concentration of 15 gpl to 35gpl respectively. The fabric finished with combination of silica nanoparticles and water repellent agent shows an increase in hydrostatic head pressure from 14.43 to 15.60 for water repellent agent concentration of 15 gpl to 35gpl respectively. This may be because of silica nanoparticles helps to resist the drop of water penetrating inside fabric structure.

4. Conclusion

This study focuses on imparting water repellent properties on 40 gsm polyester non woven fabric. For this nano silica particle was synthesized by using stober method, fabric was then finished with both water repellent agent and combination of both water repellent agent andnano silica particle. It was observed that spray rating of 70 was observed for fabric treated with water repellent agent and spray rating of 80 was observed for fabric treated with combination of both water repellent agent and nano silica particle. This indicates that the nano silica particles helps in improving water repellent properties by roughening the fabric surface. Also there was decreased in air permeability and increased in hydrostatic head pressure and decreased in tearing strength was observed as the concentration of water repellent agent increased.

5. References

1. Wang, Shutao, Jiang l., "Defination of Superhydrophobic State," Advanced Material's, 19 (2007).
2. Du Y., Li k. & Zhang J., " Application of the Water and Oil Repellent Finishing Agent EX-910E in Polyester Nonwoven," Asian Social Journal, July 2009.
3. Landage S.M., Kulkarni S.G. &Ubarhande D.P., "Synthesis and application of Silica Nanoparticles on Cotton to impart Superhydrophobicity," IJERT, Vol.1,July-2012
4. H. M. Shang, Y. Wng, K. Takahashi, G. Z. Cao, " Nanostructured superhydrophobic surfaces," Journal of Materials Science, 40, 3587-3591(2005).
5. Wenzel r.n., "Resistance of Solid Surface to Wetting by Water," (1936).
6. W. Stober, A Fink, "controlled growth of Monodisperse silica spheres in the Micron size range", Journal of colloid and interface science 26, 62-69 (1968).

Characterization Of 20 GDC Electrolyte By Bet, Tem.

Koteswararao P[1], M Buchi Suresh[2], B N Wani[3], P V Bhaskara Rao[4]

[1]Centre for Nano Science and Technology, Jawaharlal Nehru Technological University, Hyderabad,
[2]Center for Ceramic Processing, International Advanced Research Centre for Powder Metallurgy and New Materials (ARCI), Hyderabad, AP, India
[3]Bhabha Atomic Research Centre, Trombay, Mumbai
[4]Physics Department, St. Mary's Engineering College, Deshmukhi, R.R (DT)

ABSTRACT

In this study, gadolinium doped ceria electrolytes for solid oxide fuel cell application were developed based on the physiochemical properties of the powders. 20GDC nano powder with average particle size of 30nm and purity >99.99% was procured from Cottor International, Mumbai, India. The specific surface area of pure GDC was determined using Quantachrom Nova 1000e surface area analyzer in the presence of nitrogen gas. Average particle size of 20GDC powder has been calculated by using Transition Electron Microscope (TEM) and it is found to be around 30nm.

Key words: Tem, Gdc, Sofc, Ceria

Introduction

Fuel cells have received great attention as environmentally friendly and efficient to generate the electric power for both stationary and mobile applications [1]. Among the various fuel cells investigated, solid oxide fuel cells (SOFCs) have the following advantages [1–3] namely durability of the solid (rather than liquid) electrolyte materials, high energy conversion efficiency (up to 60–80%), wide variety of fuels (including hydrocarbons and oxygenates) , non-noble metal electrode and no threat from CO poisoning. Yttria stabilized zirconia (YSZ) materials are mainly used as an electrolyte due to their stability and high ionic conductivity at high temperature 1000 °C. But YSZ shows low ionic conductivity at lower temperature [4, 5]. Ceria doped with heterovalent cations, such as alkaline earth and rare earth ions, have been considered one of the most promising electrolyte materials for intermediate temperature solid oxide fuel cells (IT-SOFCs). These materials demonstrate much higher ionic conductivity at relatively low temperatures in comparison to that of YSZ. Among the various dopants studied, Gd3+ and Sm3+ singly doped ceria (abbreviated as CGO and CSO) have been reported to have the highest conductivity and to be relatively stable in thereducing environment [6-8]. This paper mainly discusses the structural characterizations of 20 % Gd doped ceria (Ce0.8Gd0.201.9 hereafter termed as 20 GDC) such as BET, TEM analysis.

2. Experimental

Purity with more than 99% of Ce0.8Gd0.201.9 (20 GDC) powder was purchased from Cottor International (Mumbai) and the powder was used to carry out the experimental studies. BET measurements were carried out for finding the surface area of the nano powder, and Particle size measured by using TEM in agreement with XRD crystallite size.

3. Bet Analysis

The specific surface area of pure GDC was determined using Quantachrom Nova 1000e surface area analyzer in the presence of nitrogen gas. Before adsorption/desorption isotherm, sample was after degassed at 300 °C for 3 hours.

	GDC 20
Surface Area	$4.858 m^2/g$
Pore Volume	0.006cc/g
Pore radius	25.894 A
Total pore volume	$7.504*10^{-03}$ cc/g

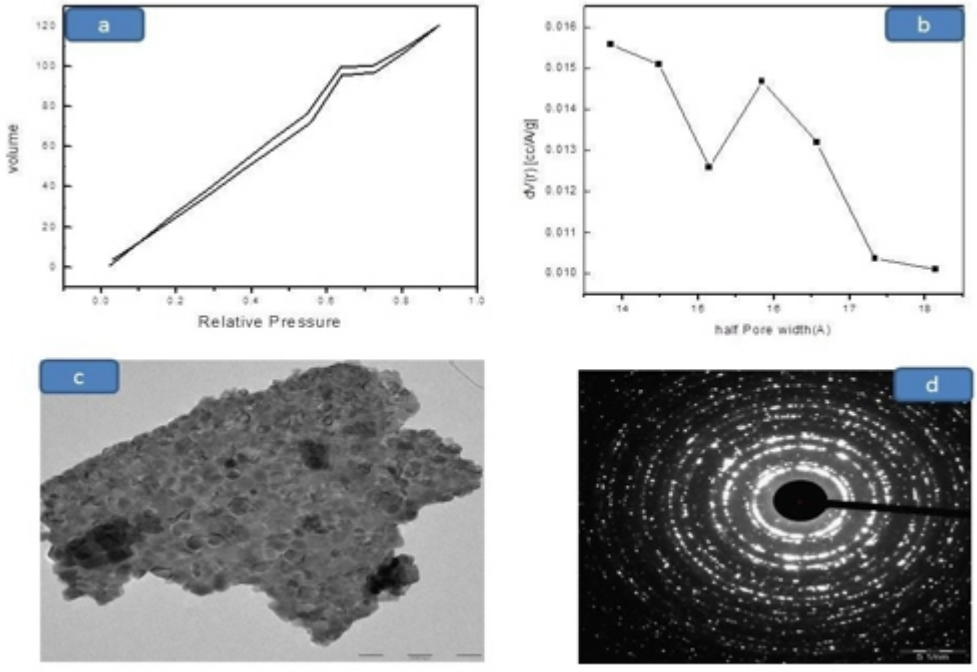

Fig 1.a) Fig shows adsorption/desorption isotherm of GDC20. Below 0.3 pressures Monolayer formation of adsorption on the material and beyond 0.7 multilayer formations is due to desorption of Nitrogen gas.

Fig 1b) shows the variation of pore volume with respect to half pore width. Pore volume is maximum at 14 half pore width .After increasing pore width, pore volume decreased again and increased up-to 16.Later on the pore volume decreased by increasing half Pore width due to Micro pore Capillary effect.

Fig 1c) shows uniform shaped nano crystals with uniform size and compacting each other due to temperature effect on Particles. The mean diameter of the individual nanoparticles measured to be - 28nm. 20 GDC powder was examined with High Magnification Transition Electron microscopy (TEM, JEOL 2010, Japhan) .

Fig:1 d) Lattice fringes visible in TEM image displayed indicate the high crystallinity of these particles. Selected area electron diffraction shown in the above figure agrees with structure of XRD results (Fluorite structure Ce fm 3m with lattice constant 5.423A)

Acknowledgment

The Author is grateful to the “Pravin Jadav’’ Research scholor Shivaji University and for providing BET facility for my samples" and is also thankful to “UGC-DAE CSR Kalpakam Centre for providing TEM facility for my samples".

References

[1] M. Sahibzada, B.C.H. Steele, K. Zheng, R.A. Rudkin, I.S. Metcalfe, Catal. Today 38 (1997) 459.
[2] M. Sahibzada, B.C.H. steele, K. Hellgardt, D. Barth, A. Effendi, D.Mantzavinos, I.S. Metcalfe, Chem. Eng.Sci. 55 (2000) 3077.
[3] R. Doshi, V.L. Richards, J.D. Carter, X. Wang, M. Krumpelt, J.Electrochem. Soc. 146 (1999) 1273.
[4] Hideaki Inaba, Hiroki Tagawa. Ceria-based solid electrolytes Review. Solid state Ionics 83(1996) 1-16.
[5] Mridula Biswas, Prashan Kumar Ojha, E Moses Jaysingh and C Durga Prasad, Synthesis ofnano crystalline Yttria Stabilized Zirconia for SOFC, Nanomaterial.Nanotechnology. 2 (2011)55-58.
[6] Yahiro H, Eguchi Y, Eguchi K, Arai H (1988) J Appl Electro-Chem 18:527
[7] Steele BCH (1989) Oxygen ion conductors. In: Takahashi T(ed) High conductivity solid ionic conductors, recent trends and applications. World Scientific, London, p 402
[8] Yahiro H, Eguchi Y, Eguchi K, Arai H (1989) Solid StateIonics 36:71

Theoretical Study Of High Temperature Superconductivity: The Case Of Cuprate ($YBa_2Cu_3O_{6.93}$)

Mequanint Assefa*, P.Singh*
* Department of Physics, Addis Ababa University, P.O.Box, 1176, Addis Ababa, Ethiopia

ABSTRACT

In this work, we determine the superconducting transition temperature and the superconducting order parameter for high temperature superconductor, particularly, for optimally doped Y $Ba_2Cu_3O_{6.93}$ analytically. In order to compute these, we have used retarded Green function method, equation of motion and Hamiltonian model. Furthermore, we obtain appropriate result which is very close to the experimental result. High temperature superconductor is very important phenomenon for changing the whole world of energy transport, and distribution as well as various scientific and technological applications.

Keywords: Superconductivity, Superconducting transition temperature, order parameter, Green function, Hamiltonian model

Introduction

Superconductivity is the ability of certain materials to conduct electricity with zero resistance below the superconducting transition temperature. This property was first discovered by Physicist Kammerling Onnes in Leiden in 1911, while cooling elemental mercury with liquid helium about 4.2K [1]. He noticed that its resistance suddenly disappeared. Superconductivity remained an empirical science for several decades. After quantum mechanics was introduced. Theorists gradually began to suspect that superconductivity was quantum phenomena.

The first widely accepted theoretical understanding of superconductivity was advanced in 1957 by American physicist John Bardeen, León Cooper and John Schrieffer [2].Their theory of superconductivity became known as the BCS theory.

In 1986 Bednorz and Muller discovered superconductivity in a lanthanum based cuprate perovskite material, transition temperature of 35K which is the high temperature superconductors [3]. In 1995,the highest temperature superconductor (at ambient pressure) is mercury barium calcium copper oxide ($HgBa_2Ca_2Cu_3O_x$), whose T_c is 135K at ambient pressure [4] and reaches 164K under high pressure [5] discovered. Cuprates remained a high priority due to its high T_c until the discovery of

superconductivity in iron-pnictides be led by Yoichi Kamihara [6] who discovered that CuO plane is not a requirement for superconductivity. In 2008, the highest superconducting transition temperature non-cuprate superconductor is pnictide ($Ca_{1-x}Nd_xFeAsF$) with $T_c = 57K$ [7].

High temperature superconductivity could revolutionize technologies ranging from magnetically-levitated trains to electrical power transmission. however, the mechanism by which these cuprate materials become superconducting and the superconducting transition temperature had remained a mystery for the last 29 years, moreover, there are different scenarios' for proposed mechanisms for high temperature superconductivity, these are exciton ,bi-exciton, polarons, bi-polarons, and magnon [8].In this paper we tried to suggest that the possible mechanism for high temperature superconductivity magnon (spin wave fluctuation) mediated superconductivity.

The paper organized as follows:

In section2, we drive equation of motion for Heisenberg operator. In Section 3 formulation of problem. We obtain the result and discussion in section 4. Lastly, in 5 conclusion of the result is given.

2. The Green function Method

In this section, we employ the basic concept of retarded Green function method as mathematical technique which is very essential to formulate problem on high temperature superconductivity. In this technique, we have tried to derive the equation of motion of operator. Green function defined for two operators a and b which do not need to be hermitian.

The Retarded Green function is defined as

$$G_r(t,t') = \ll a(t)b(t') \gg = -i\theta(t-t') < [a(t), b(t') > ----------(1)$$

Where <<…..>> represents the Green function, $\theta(t-t')$is the Heaviside step function a(t) and b(t') are annihilation and creation operators respectively

2.1 Equation Of Motion

Now let us derive the equation of motion, The Retarded Green function is

$$G_r(t,t') = \ll a(t)b(t') \gg = -i\theta(t-t') < [a(t), b(t') >$$

Differentiating eqn(1) with respect to t

$$\frac{dG_r(t,t')}{dt} = -i\frac{d\theta(t-t')}{dt} < [a(t), b(t') > -i\theta(t-t') < [\frac{da(t)}{dt}, b(t')] >$$

Applying $\frac{da(t)}{dt} = -i[a(t), H]$

We obtain

$$\omega \ll a(t)b(t') \gg = < [a(t), b(t')] > + \ll [a(t), H]b(t') \gg \text{----------(2)}$$

This the equation of motion

3. Formulation of the problem

In this section, we have tried to solve and determine the superconducting transition temperature, superconducting order parameter for optimal doped $YBa_2Cu_3O_{6.93}$ using a model Hamiltonian with Green function formalism The Hamiltonian for optimal doped $YBa_2Cu_3O_{6.93}$ is given by

$$\hat{H} = \hat{H_o} + \hat{H}_{sf} \text{----------(3)}$$

Where

$$\hat{H_0} = \sum_{k\sigma} \xi_{k\sigma} a^+_{k\sigma} a_{k\sigma} + \sum_{k\sigma} \hbar\omega\, b^+_{k\sigma} b_{k\sigma} \text{----------(4)}$$

Hamiltonian describes for itinerant and localized electrons

$$\hat{H}_{sf} = J \sum_{k\sigma,} S^{\alpha}{}_{k} \cdot \sigma^{\alpha}_{\sigma,\sigma'} a^+_{k\sigma} a_{k'\sigma} \text{----------(5)}$$

The spin-fermions interaction between two sets of electrons

Where σ represents Pauli matrix and S represents spin operator

$$\sum_{\alpha} S^{\alpha}_{k} . \sigma^{\alpha}_{\sigma,\sigma'} = S^z_k \sigma^z + S^x_k \sigma^x + S^y_k \sigma^y$$

This is reduced to

$$\sum_{\alpha} S^{\alpha}_{k} . \sigma^{\alpha}_{\sigma,\sigma'} = S^z_k \sigma^z + S^+_k \sigma^- + S^-_k \sigma^+$$

$$\hat{H}_{sf} = J \sum_{k\sigma,} [S^z_k \sigma^z + S^+_k \sigma^- + S^-_k \sigma^+] a^+_{k\sigma} a_{k'\sigma} \text{------(6)}$$

$$\hat{S}^z{}_k = \frac{1}{2} \sum_{k,k'} [a^+_{k\uparrow} a_{k'\uparrow} - a^+_{k\downarrow} a_{k'\downarrow}]$$

$$\hat{S}^{+}{}_{k} = \sum_{k\sigma,} a^{+}_{k\uparrow} a_{k'\downarrow}$$

$$\hat{S}^{-}{}_{k} = \sum_{k\sigma,} a^{+}_{k\downarrow} a_{k'\uparrow}$$

The spin $\hat{S}^{+}{}_{k}$ operator destroyed a down spin and created an up spin, while in $\hat{S}^{-}{}_{k,}$ it is the other way around. We also see that $\hat{S}^{z}{}_{k}$ counts the number of up spins minus the number of down spins

The spin-electron interaction Hamiltonian will be

$$\hat{H}_{sf} = \frac{1}{2}\sum_{k,k'} J[a^{+}_{k\uparrow} a_{k''\uparrow} - a^{+}_{k\downarrow} a_{k'\downarrow}][a^{+}_{k\uparrow} a_{k''\uparrow} - a^{+}_{k\downarrow} a_{k'\downarrow}]$$
$$+ J\sum_{k\sigma,} [a^{+}_{k\uparrow} a_{k'\downarrow}\ a^{+}_{k\downarrow} a_{k'\uparrow} + a^{+}_{k\downarrow} a_{k'\uparrow}\ a^{+}_{k\uparrow} a_{k'\downarrow}] - -(7)$$

$$\hat{H}_{sf} = \frac{1}{2}J\sum_{k,k'} [a^{+}_{k\uparrow} a_{k'\uparrow}\ a^{+}_{k\uparrow} a_{k'\uparrow} - a^{+}_{k\uparrow} a_{k'\uparrow} a^{+}_{k\downarrow} a_{k'\downarrow} - a^{+}_{k\downarrow} a_{k'\downarrow}\ a^{+}_{k\uparrow} a_{k'\uparrow} + a^{+}_{k\downarrow} a_{k'\downarrow}\ a^{+}_{k\downarrow} a_{k'\downarrow}]$$
$$+ J\sum_{k\sigma,} [a^{+}_{k\uparrow} a_{k'\downarrow}\ a^{+}_{k\downarrow} a_{k'\uparrow} + a^{+}_{k\downarrow} a_{k'\uparrow}\ a^{+}_{k\uparrow} a_{k'\downarrow}] - - - - - - - - - - (8)$$

Employing mean field approximation $\hat{H}_{sf}$

$$\hat{H}_{sf} = \frac{1}{2}J\sum_{k,k'} [< a^{+}_{k\uparrow} a^{+}_{k\uparrow} > a_{k'\uparrow} a_{k'\uparrow} + < a_{k'\uparrow} a_{k'\uparrow} > a^{+}_{k\uparrow} a^{+}_{k\uparrow} - < a^{+}_{k\uparrow} a^{+}_{k\downarrow} > a_{k'\uparrow} a_{k'\downarrow} - < a_{k\uparrow} a_{k'\downarrow}$$
$$> a^{+}_{k\uparrow} a^{+}_{k\downarrow} - < a^{+}_{k\downarrow} a^{+}_{k\uparrow} > a_{k'\downarrow} a_{k'\uparrow} - < a_{k'\downarrow} a_{k'\uparrow} > a^{+}_{k\downarrow} a^{+}_{k\uparrow} +$$
$$< a^{+}_{k\downarrow} a^{+}_{k\downarrow} > a_{k'\downarrow} a_{k'\downarrow} + < a_{k'\downarrow} a_{k'\downarrow}$$
$$> a^{+}_{k\downarrow} a^{+}_{k\downarrow}]$$
$$+ J\sum_{kk',} [< a^{+}_{k\uparrow} a^{+}_{k\downarrow} > a_{k'\downarrow} a_{k'\uparrow} + < a_{k'\downarrow} a_{k'\uparrow} > a^{+}_{k\uparrow} a^{+}_{k\downarrow} +$$
$$< a^{+}_{k\downarrow} a^{+}_{k\uparrow} > a_{k'\uparrow} a_{k'\downarrow} + < a_{k'\uparrow} a_{k'\downarrow} > a^{+}_{k\downarrow} a^{+}_{k\uparrow}] - - - - - - - - - - - - (9)$$

The superconducting order parameter is defined as

$$\Delta^{\uparrow\uparrow} = J\sum_{k\sigma,} < a_{k'\uparrow} a_{k\uparrow} >$$

$$\Delta^{\uparrow\downarrow} = J\sum_{kk',} < a_{k\uparrow} a_{k\downarrow} >$$

From equation of motion, we have

$$\omega \ll a_{k\uparrow} a^{+}_{k\uparrow} \gg = < [a_{k\uparrow}, a^{+}_{k\uparrow}] > + \ll [a_{k\uparrow}, H] a^{+}_{k\uparrow} \gg - - - - - - - - - - - - (10)$$

When we evaluate $[a_{k\uparrow}, H]$

$$[a_{k\uparrow}, H] = \xi_k \; a_{k\uparrow} + \frac{1}{2}\Delta^{\uparrow\uparrow} a^{+}_{k\uparrow} + \Delta^{\uparrow\downarrow} a^{+}_{k\downarrow} \quad ---------- (11)$$

Plugging eqn(11) into eqn(10),we obtain

$$(\omega - \xi_k) \ll a_{k\uparrow} a^{+}_{k\uparrow} \gg = 1 + \frac{1}{2}\Delta^{\uparrow\uparrow} \ll a^{+}_{k\uparrow} a^{+}_{k\uparrow} \gg - \Delta^{\uparrow\downarrow} \ll a^{+}_{k\downarrow} a^{+}_{k\uparrow} \gg \quad ---- (12)$$

Similarly

$$(\omega + \xi_k) \ll a^{+}_{k\uparrow} a^{+}_{k\uparrow} \gg = -\frac{1}{2}\Delta^{+\uparrow\uparrow} \ll a_{k'\uparrow} a^{+}_{k\uparrow} \gg - \Delta^{\uparrow\downarrow} \ll a_{k'\downarrow} a^{+}_{k\uparrow} \gg \quad ---- (13)$$

$$(\omega + \xi_k) \ll a^{+}_{k\downarrow} a^{+}_{k\uparrow} \gg = -\frac{1}{2}\Delta^{+\downarrow\downarrow} \ll a_{k'\downarrow} a^{+}_{k\uparrow} \gg - \Delta^{+\uparrow\downarrow} \ll a_{k\downarrow} a^{+}_{k\uparrow} \gg \quad ---- (14)$$

$$(\omega - \xi_k) \ll a_{k\downarrow} a^{+}_{k\uparrow} \gg = \frac{1}{2}\Delta^{\downarrow\downarrow} \ll a^{+}_{k\downarrow} a^{+}_{k\uparrow} \gg + \Delta^{\uparrow\downarrow} \ll a^{+}_{k\downarrow} a^{+}_{k\uparrow} \gg \quad ------ (15)$$

Combining eqn(12),eqn(13),eqn(14)and eqn(15),we obtain

$$\ll a^{+}_{k\uparrow} a^{+}_{k\uparrow} \gg = \frac{-\frac{\Delta^{+\uparrow\uparrow}}{2}}{(\omega^2 - \xi_k{}^2 - \frac{1}{4}(\Delta^{+\uparrow\uparrow})^2)} \quad ---------- (16)$$

The superconducting order parameter for ($\uparrow\uparrow$) is given by

$$\Delta^{+\uparrow\uparrow} = \frac{1}{\beta}\sum_{n,k} J \ll a^{+}_{k\uparrow} a^{+}_{k\uparrow} \gg \quad ---------- (17)$$

$$\Delta^{+\uparrow\uparrow} = \frac{1}{\beta}\sum_{n,} \int_0^{\infty} d\xi \, D(\xi_k) J \frac{-\frac{\Delta^{+\uparrow\uparrow}}{2}}{\left(\omega^2 - \xi_k{}^2 - \frac{1}{4}(\Delta^{+\uparrow\uparrow})^2\right)} \quad ---------- (18)$$

Applying

$\Delta(k) = \sum_{k,k'} \eta \Delta(k')$ and $D(\xi) = \eta \Delta D(0)$, For D-wave pairing $\eta = \frac{1}{2}$

$\lambda_{sf} = \sum_{k,k'} JD(0)$

Replacing $\xi^2 = \xi_k{}^2 + \frac{1}{4}(\Delta^{+\uparrow\uparrow})^2$ and $\omega_n = \frac{(2n+1)\pi}{\beta}$

$\omega = i\omega_n$ for Matsubara frequency of fermions

$$1 = \frac{\lambda_{sf}}{\beta}\sum_{n,}\int_0^{\hbar\omega} d\xi \frac{1}{((2n+1)^2\pi^2 - \beta^2\xi^2)}$$

Let $z = \beta\xi$

$$\frac{1}{\lambda_{sf}} = \frac{1}{\beta}\sum_{n,}\int_0^{\hbar\omega} d\xi \frac{1}{((2n+1)^2\pi^2 - z^2)} \text{----------(19)}$$

$$\frac{1}{\beta}\sum_{n,}\frac{1}{((2n+1)^2\pi^2 - z^2)} = \frac{\tanh\left(\frac{\beta z}{z}\right)}{2z}$$

$$\frac{1}{\lambda_{sf}} = \int_0^{\hbar\omega} d\xi \frac{\tanh\left(\beta/2\sqrt{\xi^2 + (\frac{\Delta}{4})^2}\right)}{\sqrt{\xi^2 + (\frac{\Delta}{4})^2}} \text{----------(20)}$$

1) When $T = T_c \Rightarrow \Delta = 0$ equation()becomes

$$\frac{1}{\lambda_{sf}} = \int_0^{\hbar\omega} d\xi \frac{\tanh(\frac{\beta\xi}{2})}{\xi} \text{----------(21)}$$

Integration by parts

$$\frac{1}{\lambda_{sf}} = \ln\left(\frac{\beta_c\hbar\omega}{2}\right)\tanh\left(\frac{\beta_c\hbar\omega}{2}\right) - \frac{\beta}{2}\int_0^{\hbar\omega} d\xi \frac{\ln(\frac{\beta\xi}{2})}{Cosh(\frac{\beta\xi}{2})^2} \text{----------(22)}$$

$$\frac{1}{\lambda_{sf}} = \log\left(\frac{\beta_c\hbar\omega}{2}\right) + \gamma - \log\left(\frac{\pi}{4}\right) \text{----------(23)}$$

$$T_c = \frac{\hbar\omega_m}{k_B} e^{\frac{-1}{\lambda_{sf}}} \text{----------(24)}$$

2) At finite temperature

$$\frac{1}{\lambda_{sf}} = \int_0^{\hbar\omega} d\xi \frac{\tanh\left(\beta/2\sqrt{\xi^2 + (\frac{\Delta}{4})^2}\right)}{\sqrt{\xi^2 + (\frac{\Delta}{4})^2}} \text{----------(25)}$$

Using Taylor expansion

$$\frac{1}{\lambda_{sf}} = \int_0^{\infty} d\xi \frac{\tanh\left(\beta/2\sqrt{\xi^2 + (\frac{\Delta}{4})^2}\right)}{\sqrt{\xi^2 + (\frac{\Delta}{4})^2}}$$

$$= \int_0^{\hbar\omega} d\xi \frac{\tanh(\frac{\beta\xi}{2})}{\xi} + \frac{\Delta^2}{8}\int_0^{\infty} \frac{\beta z - \sinh(\beta z)}{2z^2 Cosh^2(\frac{\beta z}{2})} --(26)$$

$$\int_0^{\infty} \frac{\beta z - \sinh(\beta z)}{2z^2 Cosh^2\left(\frac{\beta z}{2}\right)} = \frac{-14\zeta(3)}{\pi^2} ----------(27)$$

Where ζ zeta functions Employing this equation into eqn(26),we obtain

$$\frac{1}{\lambda_{sf}} = \int_0^{\infty} d\xi \frac{\tanh(\frac{\beta\xi}{2})}{\xi} + \frac{\Delta^2}{8}\left[\frac{\beta_c^2}{8}\right]\frac{-14\zeta(3)}{\pi^2} ----------(28)$$

$$\ln\left(\frac{2\beta_c \omega e^{\gamma}}{\pi}\right) = \ln\left(\frac{2\beta\omega e^{\gamma}}{\pi}\right) - \frac{14\Delta^2\zeta(3)}{64\pi^2 k_B^2 T_c^2}$$

$$\ln\left(\frac{T}{T_c}\right) = -\frac{14\Delta^2\zeta(3)}{64\pi^2 k_B^2 T_c^2} ----------(29)$$

We use approximation $e^x \approx 1 + x$, Where $x = -\frac{14\Delta^2\zeta(3)}{64\pi^2 k_B^2 T_c^2}$ and $\zeta(3) = 1.2025$

Employing this equation into

$$\Delta = 6.12 k_B T_c \sqrt{\left[1 - \frac{T}{T_c}\right]} ----------(30)$$

This is the superconducting order parameter as a function of temperature

4. Result and Discussion

This section concerned with theoretical results of high temperature superconductivity which are obtained using the equations derived in section 3.The main focus is on the superconductive transition temperature, the superconducting order parameter and coupling strength. The expression of superconducting transition temperature from eqn (24) is

$$T_c = \frac{\hbar\omega_m}{k_B} e^{\frac{-1}{\lambda_{sf}}} = 8.67X10^{-12}\omega_m \; e^{-\frac{1}{\lambda_{sf}}}$$

Now taking $\frac{\hbar\omega_m}{k_B} = 158.7K, \lambda_{sf} = 1.5$

$$\Rightarrow T_c \approx 92.4K$$

Moreover, the results of our work are best described by figures depicted below

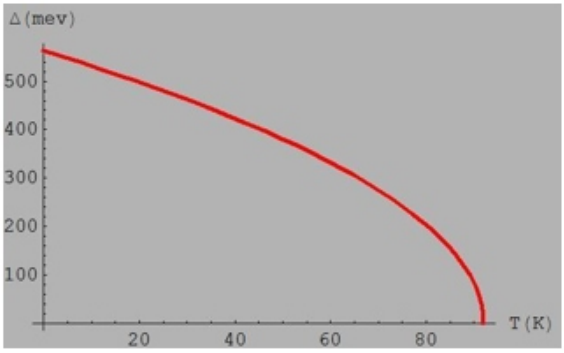

Fig1 superconducting order parameter versus temperature

From Fig .1, we can observe that the superconducting order parameter decreases monotonically as the temperature increases and vanishes at $T_c = 92.4K$. Below T_c, it is the region of superconducting state whereas above T_c, it is normal state.

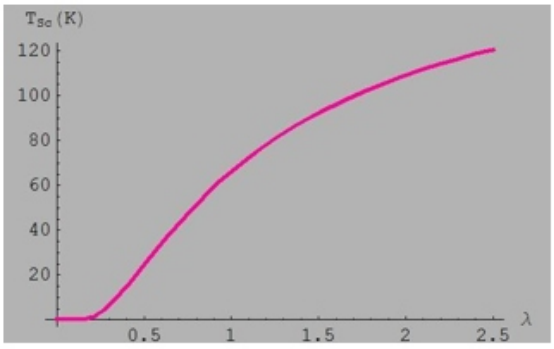

Fig2 Superconducting transition temperature versus coupling strength

The superconducting transition temperature increases as the coupling strength parameter increases and becomes slowly increase as the coupling strength parameter increases further

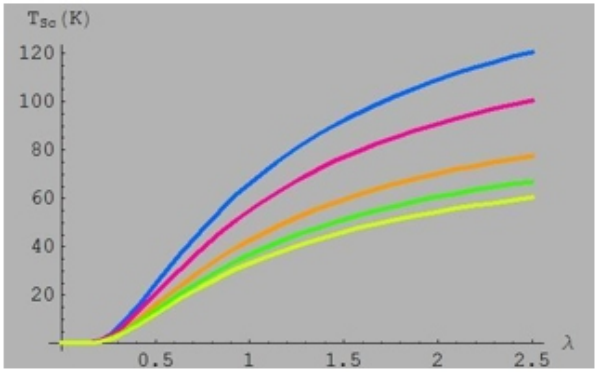

Fig3 Superconducting transition temperature versus coupling strength for different magnon frequency

5. Conclusion

In this paper, we have studied the high temperature superconductivity involving cuprate with the help of retarded Green function technique and Hamiltonian model. We have determined analytically the superconducting transition temperature for Y $Ba_2Cu_3O_{6:93}$ and the result is very close to the experiment result. We also observed that the superconducting order parameter decreases monotonically with the increasing temperature and disappear at the superconducting transition temperature for Y $Ba_2Cu_3O_{6:93}$.

6. Reference

[1] Heike Kammerling Onnes, Commn.Phys.Lab.Univ.Leiden, 12,120(1911)
[2] J.Bardeen, L.N.Coopper and J.R.Scrieffer, Phys.Rev, 108, 1175(1957)
[3] J. Bednorz, and K.A. Muller, Z.Phys.B, 64,189(1986)
[4] Schilling A.; Cantoni M.Guo, J.D.Ott, H, R.Nature, 363, 56-58(1993) [5] Gao.L.etal., Phys.Rev.B, 50, 4260-4263(1994)
[6] Y.Kamihara ,etal., J.Am.Chem.Soc.130, 3296(2008)
[7] C.Wang.etal., Eurosphys.Lett.83, 67006(2001)
[8] Singh .P, Sinha K.P, J. Solid state communication, 73, 45(1990)

Design And Performance Analysis Of CMOS Based 7T SRAM Using BIST Architecture

Deepika Rao V[1], Bhagyavathi V K 2
M.TECH. Student VLSI &EC Department KVG College of Engineering Sullia, India[1]
Associate Professor E&C Department KVG College of Engineering Sullia, India[2]

ABSTRACT

testing of VLSI components is the most time consuming and tedious work. Built in self test architecture provides capability of providing the testing with the advantage of having high fault coverage and high speed of testing. Offline and online tests are available in BIST scheme. The use of a static-RAM structure to store the relative locations of the vectors that reach the circuit inputs examined in the window. In the current technology, less area, high speed and low power consumption are the most needed factors. In any high speed circuits, Static Random Access Memories (SRAMs) has been most usually used information storage devices. In the proposed paper work, a concurrent BIST Architecture ave been used for monitoring the set of input vectors during the normal operation of SRAM. A low power consumption is made possible than the previously used system.

Keywords—storage devices, BIST, Fault coverage.

Introduction

For semiconductor integrated circuits, during the past decades, the CMOS technology emerged as the dominant fabrication method, and CMOS became the almost exclusive choice for semiconductor memory design also. Device scaling has resulted in large scale integrated, high performance, low-power, and low cost systems. CMOS memories are used in a much greater quantity than all the other types of semiconductor integrated circuits, and appear in an astounding variety of circuit organizations. With the development of CMOS memory technology numerous publications presented select memory circuit and architecture designs. [1]The literature of CMOS technology made little effort to give overview methodical analyses of some significant memory specific issues such as sense amplifiers, redundancy implementations and radiation hardening by circuit technical approaches.

SRAM cache is the first victim of increased process variations that requires handcrafted design to meet area, power, and performance requirements. Static RAM is fast, so static RAM is used to create the CPU's speed-sensitive cache. Fig 1 shows the elementary structure of a SRAM design. Since it is expensive, it is usually normally used for the applications where less memory is enough in a system. An SRAM is designed to fill two needs: First need — to provide a direct interface with the CPU at speeds not attainable by other memories like DRAM, and in the systems that require very low power

consumption. The second need — low power — is found in most portable equipments.

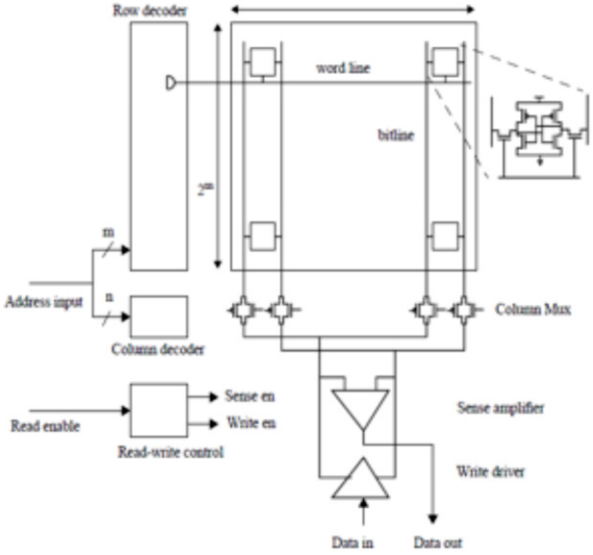

Figure 1. Elementary SRAM structure

Built-In-Self Test (BIST) techniques constitute an attractive and practical solution to the problem of testing VLSI circuits and systems. BIST techniques are classified into offline and online.[2] Offline architectures operate in either normal mode or test mode. During test mode, the inputs generated by a test generator module are applied to the inputs of the circuit under test (CUT) and the responses are captured into a response verifier (RV). Therefore, to perform the test, the normal operation of the CUT is stalled and, consequently, the performance of the system in which the circuit is included, is degraded.

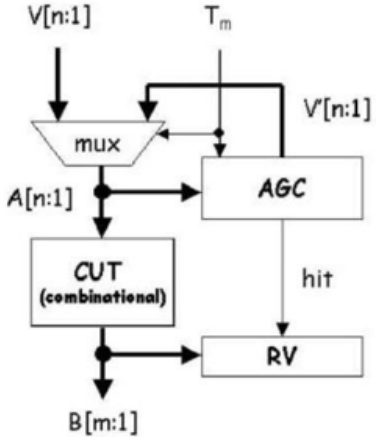

Figure 2: Input vector monitoring concurrent BIST architecture.

To avoid this performance degradation, input vector monitoring concurrent BIST techniques have been proposed which exploit input vectors arriving at the inputs of the CUT during normal operation. BIST uses a Test Pattern Generator (TPG) to generate the test patterns which are applied to the inputs of the Circuit Under Test (CUT).The block diagram of an input vector monitoring concurrent BIST technique is presented in Figure 1.

I. Literature Survey

In this project, a literature survey is cited on the combination of BIST architecture and design of SRAM's considering different transistor sizing as well as focusing on different performance parameters. In one research paper, A Built-ln Concurrent Self-Test (BICST) technique for testing combinational logic circuits concurrently with their normal operation is proposed. Concept of sharing the test hardware between identical circuits to reduce the overall area overhead is introduced. [3]The method was implemented in the design of an ALU with on-line test capability in CMOS technology. The additional hardware used for a 12-bit ALU was 19% of the total chip area and it did not impose any timing overhead on the operation of the ALU. The overhead decreases with an increase in the size of the ALU. Following the description of the BICST technique, measures for evaluating the performance of the BICST technique are defined.

[7]Due to CMOS technology scaling and the need of battery operated devices continues to drive the increase of on-die memory density to meet performance needs in various applications. Meanwhile, the device variation and leakage are increasing as the miniaturization of the transistor continues which also affects the reliability and performance of the device. As a result, it is increasingly challenging to develop SRAM with adequate stability margin for low-voltage operation while keeping the power consumption low enough to meet system-level power requirements. It is analyzed the performance of various topologies of SRAM cells at various process technologies for enhancing the cell stability which is related to the cell SNM and the leakage power consumption.

II. Proposed 7t Sram Cell With The Bist Scheme

Context below explains the working of 7T SRAM cell comprising the read, write operations, considering the performance of the device also obtaining the performance comparison with the CMOS SRAM cell.

The circuit of 7T SRAM cell consists of two inverters that are connected and cross coupled to each other with additional NMOS transistor which connected to write line (WL) and also having two pass NMOS transistors connected to bit lines (BL) and bit-lines bar (BLB) respectively. Figure 3 shows circuit of 7T SRAM Cell, where the access transistor M6 is connected to the word-line (WL) which will perform the access write and M3 is connected to the Read-line (R) to perform the read operations. Bit-lines will act as the I/O nodes carrying data from SRAM cells to a sense amplifier during read operation, or from the write input in the memory cells during write operations.

Two inverters are used, they are inv1 and inv2. 7T SRAM cell depends on the cutting off the feedback

connection between two inverters, inv1 and inv2, before any write operation takes place. The connection and disconnection of the feedback is performed by an extra NMOS transistor M7 and cell depends only on BLB to perform the write operation.

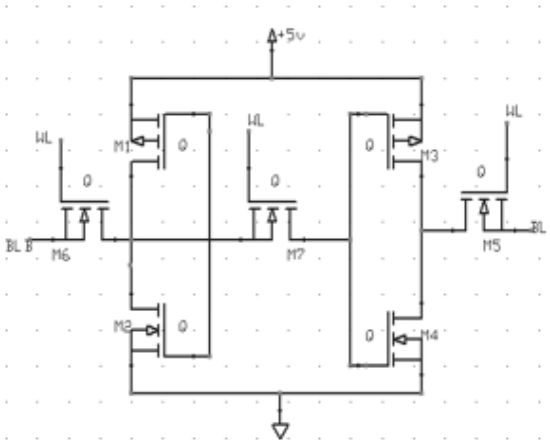

Fig 3: 7T SRAM cell

Write Operation

*4+The 7T SRAM cell's write operation starts by turning M7 off this in turn will cut off the feedback connection. BLB signal carries the complement of the input data, Q6 is turned on, while is off as shown in Figure 4. The 7T SRAM cell looks here like two cascaded inverters connected in series as shown in Figure 4. M6 is the transistor which transfers the data from BLBto which drives second set of inverters, M3 and M4, to develop the cell data.

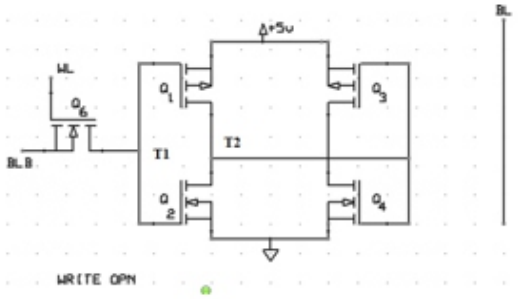

Figure 4: Write operation circuit.

Similarly, the cell data present here drives first inverter set, M1 and M2, to develop Q _bar which equals Q2 if data is “0” and lightly higher than Q2 if data is “1.” Then, Word Line is turned off and N5 is turned on to reconnect the feedback connection between the two inverters to stably store the new data. Both the bit lines (BL and BLB) are pre-charged to “high.” When the circuit is in the write mode, then BLB is kept in “high” to write “0” value having the negligible power consumption and also consideration of transistor sizing is very much essential for the stabilized write “0” operation. To store the value “1” in the cell, BLB is discharged to “0”. There is no need of discharging the bit line (BLB) to store the value of “0” in the cell.

Read Operation

In the read signal operation of the 7T SRAM cell, both the read and write signals are kept ON also the transistor Q7 kept turned ON. *9+ When the point T1 is made “0”, M2 and M5 will be turned on in the read path. The figure 5 shows the transistors available during the phase of read operation. This operation is similar to the 6T SRAM cell.

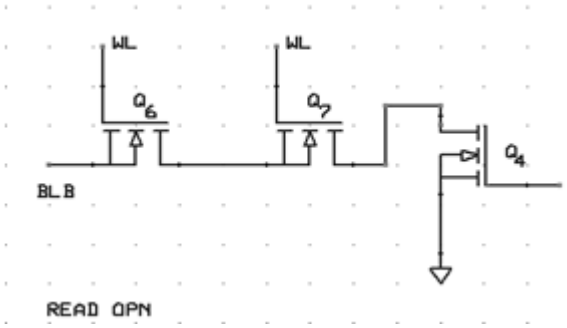

Figure 5: read operation circuit

Let us consider a combinational CUT with n input lines, from the figure 6; hence the possible input vectors for this CUT are 2n. The proposed scheme is based on the idea of monitoring a window of vectors, whose size is W, with W = 2w, where w is an integer number w < n.

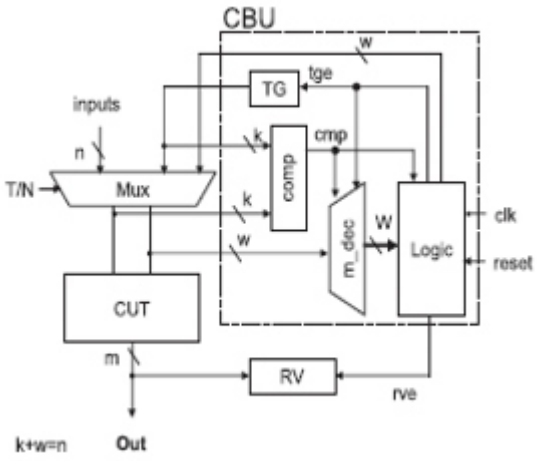

Figure 6: proposed architecture.

Every moment, the test vectors belonging to the window are monitored, and if a vector performs a hit, the RV is enabled. Proposed architecture is shown in figure 6. [5]The bits of the input vector are separated into two distinct sets comprising w and k bits, respectively, such that w + k = n. The k (high order) bits of the input vector show whether the input vector belongs to the window under consideration. The remaining bits show the relative location of the incoming vector in the current window. If the incoming vector belongs to the current window and has not been received during the examination of the current window, we say that the vector has performed a hit and the RV is clocked to

capture the CUT's response to the vector. When all vectors that belong to the current window have reached the CUT inputs, we proceed to examine the next window.

During normal mode, the inputs to the CUT are driven from the normal inputs. The n inputs are also driven to the CBU as follows: the w low-order inputs are driven to the inputs of the decoder; the k high-order inputs are driven to the inputs of the comparator. When a vector belonging to the current window reaches the inputs of the CUT, the comparator is enabled and one of the outputs of the decoder is enabled. During the first half of the clock cycle (clk and cmp are enabled) the addressed cell is read; because the read value is zero, the w-stage counter is triggered through the NOT gate with output the response verifier enable (rve) signal. During the second half of the clock cycle, the left flip-flop (the one whose clock input is inverted)enables the AND gate (whose other input is clk and cmp), and enables the buffers to write the value one to the addressed cell.

IV. Simulation And Results

The proposed Architecture circuits have been simulated using Xilinx13.2 tool. Also we have used ModelSim SE as a verification tool which provides High Performance Simulation and Debug. ModelSim SE is our UNIX, Linux, and Windows-based simulation and debug environment, combining high performance with the most powerful and intuitive GUI in the industry.

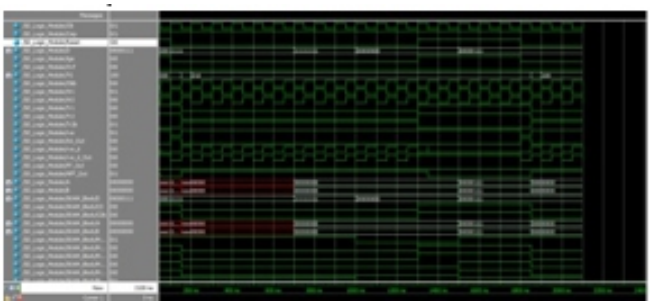

Figure 7: Logic module

XilinxISE (Integrated Software Environment) is a software tool produced by Xilinx for synthesis and analysis of HDL designs, enabling the developer to synthesize (compile) their designs, perform timing analysis, examine RTL diagrams, simulate a design's reaction to different stimuli, and configure the target device with the programmer.

During the write cycle the operation consumes power of 0.7μW with the consumption of 0.5μA. the read operation for each cell requires 0.06μW of power and 0.10μA of current.

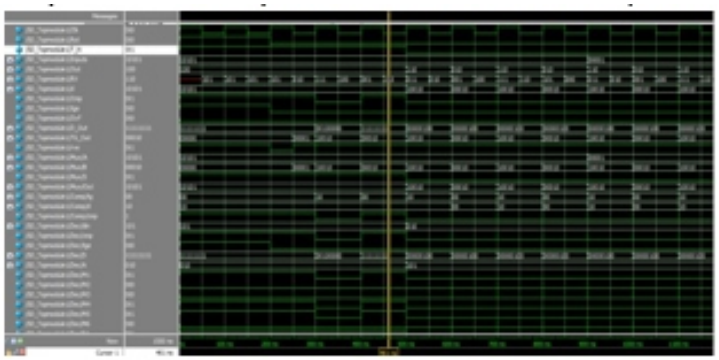

Figure 8: top module

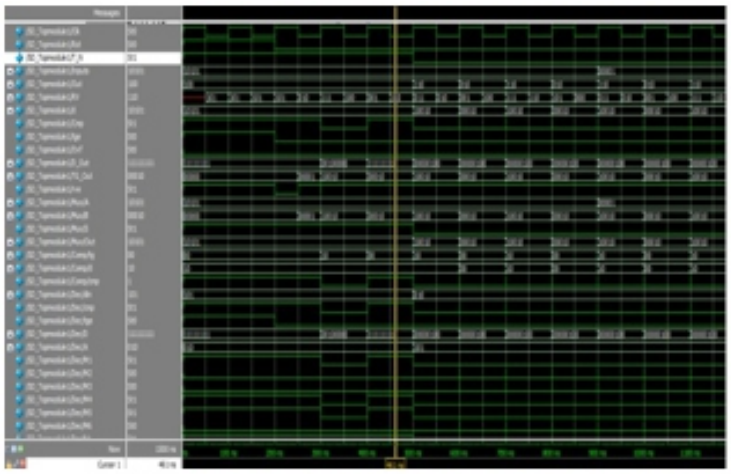

Figure 9: response verifier

IV. Conclusion And Future Work

In the paper, it is discussed about the BIST schemes which constitute an attractive solution to the problem of testing VLSI devices. Input vector monitoring concurrent BIST schemes perform testing during the circuit normal operation without imposing a need to set the circuit offline to perform the test, therefore they can circumvent problems appearing in offline BIST techniques. The evaluation criteria for this class of schemes are the hardware overhead and the CTL, i.e., the time required for the test to complete, while the circuit operates normally. In this brief, a novel input vector monitoring concurrent BIST architecture has been presented. It is proven that the device speeds up to 23% faster than the normal operating device.

References

*[1]Low Power Design and Simulation of 7T SRAM Cell using various Circuit Techniques Pankaj Agarwal, Nikhil Saxena*2, Nikhita Tripathi*3International Journal of Engineering Trends and Technology (IJETT) Volume4Issue5- May 2013*

[2]. Voyiatzis, A. Paschalis, D. Gizopoulos, N. Kranitis, and C.Halatsis, "A concurrent BIST architecture based on a selftestingRAM," IEEE Trans. Rel., vol. 54, no. 1, pp. 69–78,Mar. 2005.

[3] E. J. McCluskey, "Built-in self-test techniques," IEEE Design TestComput., vol. 2, no. 2, pp. 21–28, Apr. 1985.

[4] SNM Analysis During Read Operation Of 7T SRAM Cells In 45nm Technology For Increase Cell Stability Deependra Singh Rajput, Manoj Kumar Yadav, Pooja Johri, Amit S. Rajput, International Journal of Engineering Research and Applications (IJERA) ISSN: 2248-9622 www.ijera.com Vol. 2, Issue4, July- August 2012, pp.2112-2117

[5] Input Vector Monitoring Concurrent BIST Architecture Using SRAM Cells Ioannis Voyiatzis and Costas Efstathiou IEEE transactions on very large scale integration (vlsi) systems, vol. 22, no. 7, july 2014

Instructions for Authors

Essentials for Publishing in this Journal

1 Submitted articles should not have been previously published or be currently under consideration for publication elsewhere.

2 Conference papers may only be submitted if the paper has been completely re-written (taken to mean more than 50%) and the author has cleared any necessary permission with the copyright owner if it has been previously copyrighted.

3 All our articles are refereed through a double-blind process.

4 All authors must declare they have read and agreed to the content of the submitted article and must sign a declaration correspond to the originality of the article.

Submission Process

All articles for this journal must be submitted using our online submissions system. http://enrichedpub.com/ . Please use the Submit Your Article link in the Author Service area.

-

Manuscript Guidelines

The instructions to authors about the article preparation for publication in the Manuscripts are submitted online, through the e-Ur (Electronic editing) system, developed by **Enriched Publications Pvt. Ltd**. The article should contain the abstract with keywords, introduction, body, conclusion, references and the summary in English language (without heading and subheading enumeration). The article length should not exceed 16 pages of A4 paper format.

Title

The title should be informative. It is in both Journal's and author's best interest to use terms suitable. For indexing and word search. If there are no such terms in the title, the author is strongly advised to add a subtitle. The title should be given in English as well. The titles precede the abstract and the summary in an appropriate language.

Letterhead Title

The letterhead title is given at a top of each page for easier identification of article copies in an Electronic form in particular. It contains the author's surname and first name initial .article title, journal title and collation (year, volume, and issue, first and last page). The journal and article titles can be given in a shortened form.

Author's Name

Full name(s) of author(s) should be used. It is advisable to give the middle initial. Names are given in their original form.

Contact Details

The postal address or the e-mail address of the author (usually of the first one if there are more Authors) is given in the footnote at the bottom of the first page.

Type of Articles

Classification of articles is a duty of the editorial staff and is of special importance. Referees and the members of the editorial staff, or section editors, can propose a category, but the editor-in-chief has the sole responsibility for their classification. Journal articles are classified as follows:

Scientific articles:

1. Original scientific paper (giving the previously unpublished results of the author's own research based on management methods).

2. Survey paper (giving an original, detailed and critical view of a research problem or an area to which the author has made a contribution visible through his self-citation);

3. Short or preliminary communication (original management paper of full format but of a smaller extent or of a preliminary character);

4. Scientific critique or forum (discussion on a particular scientific topic, based exclusively on management argumentation) and commentaries. Exceptionally, in particular areas, a scientific paper in the Journal can be in a form of a monograph or a critical edition of scientific data (historical, archival, lexicographic, bibliographic, data survey, etc.) which were unknown or hardly accessible for scientific research.

Professional articles:

1. Professional paper (contribution offering experience useful for improvement of professional practice but not necessarily based on scientific methods);
2. Informative contribution (editorial, commentary, etc.);
3. Review (of a book, software, case study, scientific event, etc.)

Language

The article should be in English. The grammar and style of the article should be of good quality. The systematized text should be without abbreviations (except standard ones). All measurements must be in SI units. The sequence of formulae is denoted in Arabic numerals in parentheses on the right-hand side.

Abstract and Summary

An abstract is a concise informative presentation of the article content for fast and accurate Evaluation of its relevance. It is both in the Editorial Office's and the author's best interest for an abstract to contain terms often used for indexing and article search. The abstract describes the purpose of the study and the methods, outlines the findings and state the conclusions. A 100- to 250-Word abstract should be placed between the title and the keywords with the body text to follow. Besides an abstract are advised to have a summary in English, at the end of the article, after the Reference list. The summary should be structured and long up to 1/10 of the article length (it is more extensive than the abstract).

Keywords

Keywords are terms or phrases showing adequately the article content for indexing and search purposes. They should be allocated heaving in mind widely accepted international sources (index, dictionary or thesaurus), such as the Web of Science keyword list for science in general. The higher their usage frequency is the better. Up to 10 keywords immediately follow the abstract and the summary, in respective languages.

Acknowledgements

The name and the number of the project or programmed within which the article was realized is given in a separate note at the bottom of the first page together with the name of the institution which financially supported the project or programmed.

Tables and Illustrations

All the captions should be in the original language as well as in English, together with the texts in illustrations if possible. Tables are typed in the same style as the text and are denoted by numerals at the top. Photographs and drawings, placed appropriately in the text, should be clear, precise and suitable for reproduction. Drawings should be created in Word or Corel.

Citation in the Text

Citation in the text must be uniform. When citing references in the text, use the reference number set in square brackets from the Reference list at the end of the article.

Footnotes

Footnotes are given at the bottom of the page with the text they refer to. They can contain less relevant details, additional explanations or used sources (e.g. scientific material, manuals). They cannot replace the cited literature.
The article should be accompanied with a cover letter with the information about the author(s): surname, middle initial, first name, and citizen personal number, rank, title, e-mail address, and affiliation address, home address including municipality, phone number in the office and at home (or a mobile phone number). The cover letter should state the type of the article and tell which illustrations are original and which are not.

Address of the Editorial Office:

Enriched Publications Pvt. Ltd.
S-9,IInd FLOOR, MLU POCKET,
MANISH ABHINAV PLAZA-II, ABOVE FEDERAL BANK,
PLOT NO-5, SECTOR -5, DWARKA, NEW DELHI, INDIA-110075,
PHONE: - + (91)-(11)-45525005

Notes: